

9. Trujillo Bueno, J., Collados, M., Paletou, F. & Molodij, G. in *Advanced Solar Polarimetry: Theory, Observations and Instrumentation* (ed. Sigwarth, M.) 141–149 (ASP Conf. Ser. Vol. 236, Astronomical Society of the Pacific, San Francisco, 2001).
10. Bomnier, V. & Molodij, G. Some THEMIS-MTR observations of the second solar spectrum (2000 campaign). *Astron. Astrophys.* **381**, 241–252 (2002).
11. Gandorfer, A. *The Second Solar Spectrum* Vol. 1, 4625 Å to 6995 Å (vdf, Zurich, 2000).
12. Faurobert-Scholl, M., Feautrier, N., Machefert, F., Petrovay, K. & Spielfiedel, A. Turbulent magnetic fields in the solar photosphere: diagnostics and interpretation. *Astron. Astrophys.* **298**, 289–302 (1995).
13. Faurobert, M., Arnaud, J., Vigneau, J. & Frisch, H. Investigation of weak solar magnetic fields. New observational results for the Sr I 460.7 nm linear polarization and radiative transfer modeling. *Astron. Astrophys.* **378**, 627–634 (2001).
14. Hanle, W. Über magnetische Beeinflussung der Polarisation der Resonanzfluoreszenz. *Z. Phys.* **30**, 93–105 (1924).
15. Trujillo Bueno, J. in *Advanced Solar Polarimetry: Theory, Observations and Instrumentation* (ed. Sigwarth, M.) 161–195 (ASP Conf. Ser. Vol. 236, Astronomical Society of the Pacific, San Francisco, 2001).
16. Stenflo, J. O. The Hanle effect and the diagnostics of turbulent magnetic fields in the solar atmosphere. *Sol. Phys.* **80**, 209–226 (1982).
17. Shchukina, N. & Trujillo Bueno, J. in *Solar Polarization 3* (eds Trujillo Bueno, J. & Sánchez Almeida, J.) 336–343 (ASP Conf. Ser. Vol. 307, Astronomical Society of the Pacific, San Francisco, 2003).
18. Asplund, M., Nordlund, Å., Trampedach, R., Allende Prieto, C. & Stein, R. F. Line formation in solar granulation. I. Fe line shapes, shifts and asymmetries. *Astron. Astrophys.* **359**, 729–742 (2000).
19. Cattaneo, F. On the origin of magnetic fields in the quiet photosphere. *Astrophys. J.* **515**, L39–L42 (1999).
20. Stein, R. F. & Nordlund, Å. in *Modelling of Stellar Atmospheres* (eds Piskunov, N. E., Weiss, W. W. & Gray, D. F.), 169–180 (ASP Conf. Ser. Vol. IAU 210, Astronomical Society of the Pacific, San Francisco, 2003).
21. Socas-Navarro, H. & Sánchez Almeida, J. Magnetic fields in the quiet Sun: observational discrepancies and unresolved structure. *Astrophys. J.* **593**, 581–586 (2003).
22. Sánchez Almeida, J., Emonet, T. & Cattaneo, F. Polarization of photospheric lines from turbulent dynamo simulations. *Astrophys. J.* **585**, 536–552 (2003).
23. Trujillo Bueno, J., Casini, R., Landolfi, M. & Landi Degl'Innocenti, E. The physical origin of the scattering polarization of the Na I D lines in the presence of weak magnetic fields. *Astrophys. J.* **566**, L53–L57 (2002).
24. Landi Degl'Innocenti, E. Evidence against turbulent and canopy-like magnetic fields in the solar chromosphere. *Nature* **392**, 256–258 (1998).
25. Stenflo, J. O. in *Solar Polarization 3* (eds Trujillo Bueno, J. & Sánchez Almeida, J.) 385–398 (ASP Conf. Ser. Vol. 307, Astronomical Society of the Pacific, San Francisco, 2003).
26. Anderson, L. S. & Athay, R. G. Model solar chromosphere with prescribed heating. *Astrophys. J.* **346**, 1010–1018 (1989).
27. Priest, E. & Forbes, T. *Magnetic Reconnection: MHD Theory and Applications* (Cambridge Univ. Press, New York, 2000).
28. Landi Degl'Innocenti, E. Polarization in spectral lines: I. A unifying theoretical approach. *Sol. Phys.* **85**, 3–31 (1983).
29. Trujillo Bueno, J. in *Stellar Atmosphere Modeling* (eds Hubeny, I., Mihalas, D. & Werner, K.) 551–582 (ASP Conf. Ser. Vol. 288, Astronomical Society of the Pacific, San Francisco, 2003).
30. Trujillo Bueno, J. in *Solar Polarization 3* (eds Trujillo Bueno, J. & Sánchez Almeida, J.) 407–424 (ASP Conf. Ser. Vol. 307, Astronomical Society of the Pacific, San Francisco, 2003).

**Acknowledgements** We thank F. Kneer, E. Landi Degl'Innocenti and F. Moreno-Insertis for scientific discussions. We are also grateful to P. Fabiani Bendicho for help with the numerical solution of the 3D radiative transfer equation. This research was supported by the Spanish Plan Nacional de Astronomía y Astrofísica and by the European Commission via the INTAS programme and the Solar Magnetism Network.

**Competing interests statement** The authors declare that they have no competing financial interests.

**Correspondence** and requests for materials should be addressed to J.T.B. (jtb@iac.es).

## Single spin detection by magnetic resonance force microscopy

D. Rugar, R. Budakian, H. J. Mamin & B. W. Chui

IBM Research Division, Almaden Research Center, 650 Harry Rd, San Jose, California 95120, USA

Magnetic resonance imaging (MRI) is well known as a powerful technique for visualizing subsurface structures with three-dimensional spatial resolution. Pushing the resolution below 1 μm remains a major challenge, however, owing to the sensitivity limitations of conventional inductive detection techniques. Currently, the smallest volume elements in an image must contain at least 10<sup>12</sup> nuclear spins for MRI-based microscopy<sup>1</sup>, or 10<sup>7</sup>

electron spins for electron spin resonance microscopy<sup>2</sup>. Magnetic resonance force microscopy (MRFM) was proposed as a means to improve detection sensitivity to the single-spin level, and thus enable three-dimensional imaging of macromolecules (for example, proteins) with atomic resolution<sup>3,4</sup>. MRFM has also been proposed as a qubit readout device for spin-based quantum computers<sup>5,6</sup>. Here we report the detection of an individual electron spin by MRFM. A spatial resolution of 25 nm in one dimension was obtained for an unpaired spin in silicon dioxide. The measured signal is consistent with a model in which the spin is aligned parallel or anti-parallel to the effective field, with a rotating-frame relaxation time of 760 ms. The long relaxation time suggests that the state of an individual spin can be monitored for extended periods of time, even while subjected to a complex set of manipulations that are part of the MRFM measurement protocol.

MRFM is based on the detection of the magnetic force between a ferromagnetic tip and spins in a sample. The fundamental challenge in achieving single-spin sensitivity is that the force from a single spin is exceedingly small. Even with tip field gradients in the gauss per nanometre range, the force from an electron spin is only a few attonewtons. This force is roughly a million times smaller than is typically detected by atomic force microscopy (AFM). Recently, major strides towards single-spin detection have been made with the development of ultrasensitive cantilever-based force sensors<sup>7,8</sup>, better understanding of relevant spin relaxation processes<sup>9–12</sup> and the successful detection of statistical polarization in small spin ensembles<sup>13</sup>.

The basic elements of our MRFM apparatus are shown in Fig. 1 and have been described in detail in ref. 13. Briefly, a custom-fabricated mass-loaded silicon cantilever<sup>8,13</sup> with an attached 150-nm-wide SmCo magnetic tip is used to sense the force from the electron spin. The sample consists of vitreous silica (Suprasil W2) that was irradiated with a 2-Gy dose of Co<sup>60</sup> gamma rays. The gamma irradiation produces a low concentration of silicon dangling bonds containing unpaired electron spins known as E' centres<sup>14</sup>.

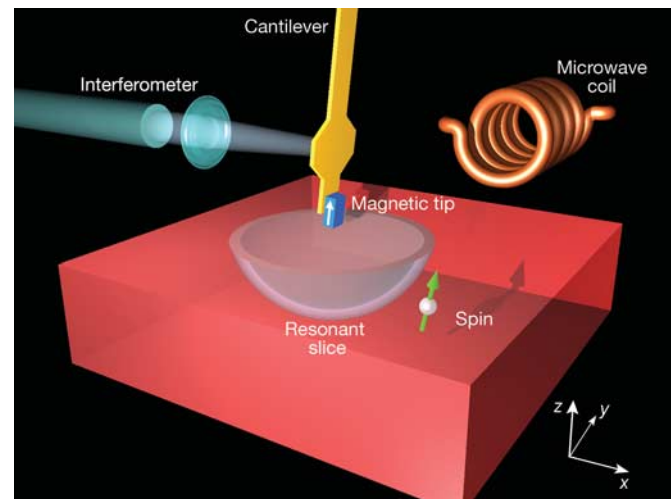


**Figure 1** Configuration of the single-spin MRFM experiment. The magnetic tip at the end of an ultrasensitive silicon cantilever is positioned approximately 125 nm above a polished SiO<sub>2</sub> sample containing a low density of unpaired electron spins. The resonant slice represents those points in the sample where the field from the magnetic tip (plus an external field) matches the condition for magnetic resonance. As the cantilever vibrates, the resonant slice swings back and forth through the sample causing cyclic adiabatic inversion of the spin. The cyclic spin inversion causes a slight shift of the cantilever frequency owing to the magnetic force exerted by the spin on the tip. Spins as deep as 100 nm below the sample surface can be probed.

Estimated spin concentration was between  $10^{13}$  and  $10^{14} \text{ cm}^{-3}$ . The experiments were performed at 1.6 K in a small vacuum chamber that fits within the bore of a superconducting magnet. The low operating temperature minimizes the force noise and reduces the relaxation rate of the spins.

A microwave magnetic field ( $B_1 \approx 0.3 \text{ mT}$ ), in combination with the inhomogeneous field from the magnetic tip, sets up a ‘resonant slice’ within the sample. The resonant slice corresponds to those points in the sample where the tip field  $\mathbf{B}_{\text{tip}}(x, y, z)$ , plus a static external field  $\hat{z} B_{\text{ext}}$ , satisfies the condition for electron spin resonance:  $B_0(x, y, z) \equiv |\mathbf{B}_{\text{tip}}(x, y, z) + \hat{z} B_{\text{ext}}| = \omega_{\text{rf}}/\gamma$ . Here,  $\omega_{\text{rf}}$  is the frequency of the microwave field and  $\gamma$  is the gyromagnetic ratio ( $\gamma/2\pi = 2.8 \times 10^{10} \text{ Hz T}^{-1}$ ). In the present experiment, where  $\omega_{\text{rf}}/2\pi = 2.96 \text{ GHz}$ , the resonant slice corresponds to  $B_0(x, y, z) = 106 \text{ mT}$ . For typical conditions (for example,  $B_{\text{ext}} = 30 \text{ mT}$ ), the slice is a bowl-shaped surface that extends roughly 250 nm below the tip. Note that with the perpendicular cantilever orientation shown in Fig. 1, the cantilever is responsive only to the  $x$  component of force. Thus the spin must be located either slightly in front of or slightly behind the cantilever in the  $x$  direction to produce a substantial response.

To generate a force signal that can be distinguished from the much larger background force fluctuations, we use the recently developed spin manipulation protocol known as ‘interrupted OSCAR’ or iOSCAR, where OSCAR stands for oscillating cantilever-driven adiabatic reversals<sup>13</sup>. In the iOSCAR protocol, the cantilever is part of a gain-controlled positive-feedback loop that drives the cantilever to oscillate at a set amplitude (for example, 16 nm) at the fundamental frequency of the cantilever ( $f_c = 5.5 \text{ kHz}$ ). Because the cantilever is the frequency-determining element in the feedback loop, the vibration frequency will automatically vary in response to tip-sample interactions<sup>15</sup>.

The vibration of the cantilever tip causes the resonant slice to sweep back and forth rapidly through the sample. If the slice happens to sweep through the location of a spin, the spin will be cyclically inverted in synchrony with the cantilever motion owing to the phenomenon of adiabatic rapid passage<sup>13,16</sup>. This synchronous inversion of the spin creates an alternating magnetic force on the cantilever that mimics a change in cantilever stiffness. The resulting shift in cantilever frequency is given by<sup>13,17</sup>:

$$\delta f_c = \pm \frac{2f_c G \mu_B}{\pi k x_{\text{peak}}} \quad (1)$$

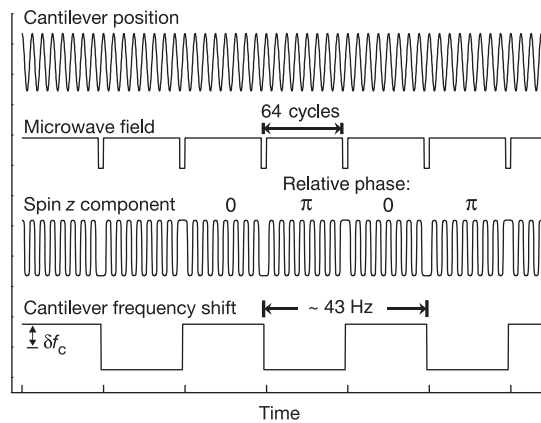


**Figure 2** Timing diagram for the iOSCAR spin manipulation protocol. The  $z$  component of spin follows the motion of the cantilever except during the interruption of the microwave field. The interruptions last for one-half of a cantilever period and are precisely timed to start and stop at vibration extrema. The interruptions, which occur every 64 cantilever cycles, reverse the phase of the spin with respect to the cantilever, resulting in a square-wave oscillation of the cantilever frequency.

where  $k$  is the cantilever spring constant,  $x_{\text{peak}}$  is the peak vibration amplitude of the cantilever,  $G \equiv \partial B_0/\partial x$  is the lateral field gradient, and  $\mu_B$  is the magnetic moment of the electron ( $9.3 \times 10^{-24} \text{ J T}^{-1}$ ). The sign of the frequency shift depends on the relative phase of the spin inversions with respect to the cantilever motion. Using the terminology of magnetic resonance, the two polarities correspond to adiabatic rapid passages with the spin either aligned or anti-aligned with respect to the effective field in the rotating frame<sup>13,16</sup>. This parallel or anti-parallel alignment is expected to be enforced by the quantum-mechanical measurement process, resulting in the collapse of the initial spin wavefunction onto an eigenstate of the effective field<sup>18,19</sup>. For the parameters of the current experiment ( $G = 2 \times 10^5 \text{ T m}^{-1}$ ;  $k = 0.11 \text{ mN m}^{-1}$ ;  $x_{\text{peak}} = 16 \text{ nm}$ ), the expected frequency shift is  $|\delta f_c| = 3.7 \pm 1.3 \text{ mHz}$ . The estimated uncertainty in  $|\delta f_c|$  reflects 20% uncertainties in the calibration of  $G$ ,  $k$  and  $x_{\text{peak}}$ .

In the ‘interrupted’ version of the protocol (iOSCAR), the microwave field  $B_1$  is turned off for one-half of a cantilever cycle every 64 cycles ( $f_{\text{int}} = f_c/64 \approx 86 \text{ Hz}$ ). As shown in Fig. 2, each time  $B_1$  is interrupted, the relative phase of the spin and cantilever is reversed, causing the frequency shift to reverse polarity. (See Supplementary Information for an animation.) The net result of the interruptions is that the frequency shift will alternate between positive and negative values in a square-wave-like fashion with a frequency given by  $f_{\text{sig}} = f_{\text{int}}/2$ , or approximately 43 Hz. The resulting frequency shift signal can be written as the Fourier series:

$$\Delta f(t) = \frac{4}{\pi} |\delta f_c| A(t) \sin(2\pi f_{\text{sig}} t) + \text{higher harmonics} \quad (2)$$

where the  $4/\pi$  comes from the first harmonic Fourier amplitude of a square wave.

We have included the function  $A(t)$  to take into account the fact that the signal will not be perfectly periodic owing to extra random spin flips induced by the environment. Assuming that this ‘quantum jump’ model is correct,  $A(t)$  is a random telegraph function that takes on values of  $\pm 1$ . For Poisson distributed jumps,  $A(t)$  is expected to have a lorentzian power spectrum<sup>20</sup> and the statistical properties  $\langle A(t) \rangle = 0$  and  $\langle [A(t)]^2 \rangle = 1$ , where  $\langle \dots \rangle$  denotes time average. We detect the first harmonic of the signal only, so we will

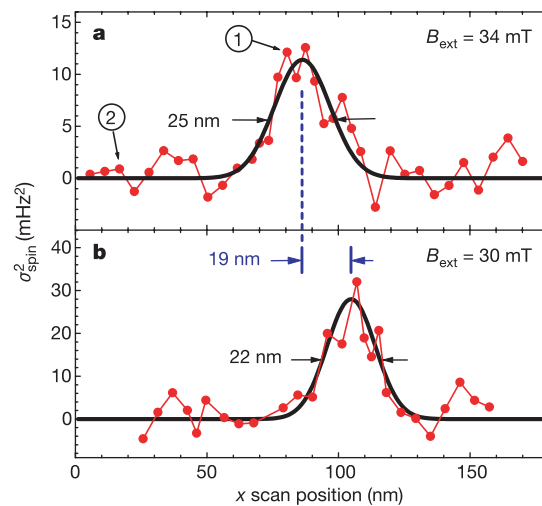


**Figure 3** Plots showing the spin signal as the sample was scanned laterally in the  $x$  direction for two values of external field: **a**,  $B_{\text{ext}} = 34 \text{ mT}$ , and **b**,  $B_{\text{ext}} = 30 \text{ mT}$ . The smooth curves are gaussian fits that serve as guides to the eye. The 19-nm shift in peak position reflects the movement of the resonant slice induced by the 4-mT change in external field. The difference in absolute peak height is primarily due to different lock-in amplifier detection bandwidths: 0.18 Hz and 0.59 Hz for **a** and **b**, respectively. Power spectra for the points marked 1 and 2 are shown in Fig. 4.

refer to the quantity  $\Delta f_1(t) \equiv (4/\pi)|\delta f_c|A(t)$  as the spin signal amplitude.

Because the frequency modulation due to the spin is only a few millihertz and the frequency noise of the cantilever due to thermal motion and tip-sample interactions is relatively large ( $\sim 25$  mHz in a 1-Hz bandwidth), we must use signal averaging to detect the spin signal. However, because  $\langle \Delta f_1(t) \rangle = 0$ , we average the square of the signal (the signal 'energy'), rather than the signal amplitude. Specifically, the frequency modulation of the cantilever is detected using an analogue frequency discriminator<sup>15</sup> followed by a digital lock-in amplifier that has been implemented in software. The lock-in amplifier uses a bank of low-pass filters and, as a function of detection bandwidth, determines the energy (that is, variance) of the in-phase and quadrature components of the frequency-shift signal  $\Delta f(t)$ . The spin signal and the measurement noise are uncorrelated, so we can write the in-phase variance as  $\sigma_I^2 = \sigma_{\text{spin}}^2 + \sigma_{\text{noise}}^2$ , where  $\sigma_{\text{spin}}^2$  is the variance due to the spin signal and  $\sigma_{\text{noise}}^2$  represents the measurement noise. This in-phase variance is then compared to the quadrature variance  $\sigma_Q^2$ , which contains only the measurement noise. The signal energy from the spin can then be estimated as  $\sigma_{\text{spin}}^2 = \sigma_I^2 - \sigma_Q^2$ . This energy detection scheme

is believed to have performance close to the theoretically optimal detector<sup>21</sup>.

Figure 3a shows a lateral scan where we plot  $\sigma_{\text{spin}}^2$  as a function of sample position. The scan shows a prominent peak that we believe is due to a single spin. The peak width is 25 nm, or roughly 1.6 times the cantilever oscillation amplitude. Note that the baseline of the data on either side of the peak is essentially zero (within the uncertainty of the measurement), thus demonstrating that the iOSCAR protocol generates no systematic feedthrough artefacts. Because the signal-to-noise ratio was so low ( $\sigma_{\text{spin}}^2/\sigma_I^2 \sim 0.06$ ), considerable averaging was required. In Fig. 3a, the averaging time was 13 h per point, yielding a signal peak that is five standard deviations above the baseline noise.

To confirm that the observed signal is truly due to magnetic resonance, a number of basic tests were performed. As expected for an iOSCAR magnetic resonance signal, the signal disappeared if the microwaves were absent or turned on continuously. The timing of the microwave interruptions was also varied. The signal disappeared, as expected, when the starting time of the interruption was shifted from the vibration peak to the zero-crossing of the vibration (that is, shifted by one-quarter of a cantilever cycle) and when the interruption duration was a full cantilever cycle instead of one-half cycle.

One key test for magnetic resonance is to observe the field dependence of the spin signal. If the external field is reduced, the resonant slice will shrink in radius, thus shifting the scan position of the signal peak. When  $B_{\text{ext}}$  was reduced from 34 to 30 mT, the expected peak shift was indeed observed and found to be  $\Delta x = 19$  nm, as can be seen by comparing the scans in Figs 3a and b. The ratio  $\Delta B_{\text{ext}}/\Delta x$  suggests that the field gradient  $G$  is approximately  $2 \times 10^5 \text{ T m}^{-1}$  ( $2 \text{ G nm}^{-1}$ ).

The conclusion that the signal is due to only one spin is based primarily on the spatial isolation of the spin signal. By design, the spin density of the sample was very low, in the range of  $10^{13}$  to  $10^{14} \text{ cm}^{-3}$ , giving a mean spacing between spins in the range of 200 to 500 nm. The sparseness of spins implies that, for most sample locations, there is no spin interacting with the resonant slice. This is why the data in Fig. 3 has a zero baseline. To locate a spin signal, the sample was scanned through many independent locations, of the order of 30, before a strong signal from a well-positioned spin was found.

By measuring  $\sigma_{\text{spin}}^2$  as a function of detection bandwidth, the power spectral density of the spin signal amplitude  $\Delta f_1(t)$  can be determined (Fig. 4a). Consistent with a random telegraph model of  $\Delta f_1(t)$ , the spectrum is well fitted by the lorentzian function  $S(f) = 4\tau_m \langle [\Delta f_1(t)]^2 \rangle / [1 + 4\pi^2 \tau_m^2 f^2]$ . The spectral width at half-maximum is 0.21 Hz, corresponding to an impressively long  $\tau_m$  correlation time of 760 ms. This is essentially the rotating frame relaxation time, but also includes possible effects of the iOSCAR spin manipulation. The long correlation time implies that the cantilever-driven spin inversions are coherent for thousands of cycles. The false-colour image in Fig. 4b shows that the spin signal is highly localized both spatially and spectrally.

The total magnitude of the spin signal, obtained by integrating the spectrum in Fig. 4a, was found to be  $\langle [\Delta f_1(t)]^2 \rangle = 28 \text{ mHz}^2$ . Using this experimental value and the relationship  $\langle [\Delta f_1(t)]^2 \rangle = (4/\pi)^2 |\delta f_c|^2 \langle [A(t)]^2 \rangle$ , we solve for  $|\delta f_c|$  using the assumption that  $\langle [A(t)]^2 \rangle = 1$ . We find  $|\delta f_c| = 4.2 \text{ mHz}$ , in excellent agreement with the value of 3.7 mHz expected from equation (1).

In conclusion, we have presented evidence that MRFM is now capable of detecting individual electron spins. Although several other single-spin detection methods have been previously demonstrated<sup>22–28</sup>, MRFM has some attributes that set it apart. Perhaps the most important of these is the ability to image spins below the surface with nanometre spatial resolution. Spins as deep as 100 nm should be accessible under present operating conditions. Although extensive signal averaging is currently required, even a modest

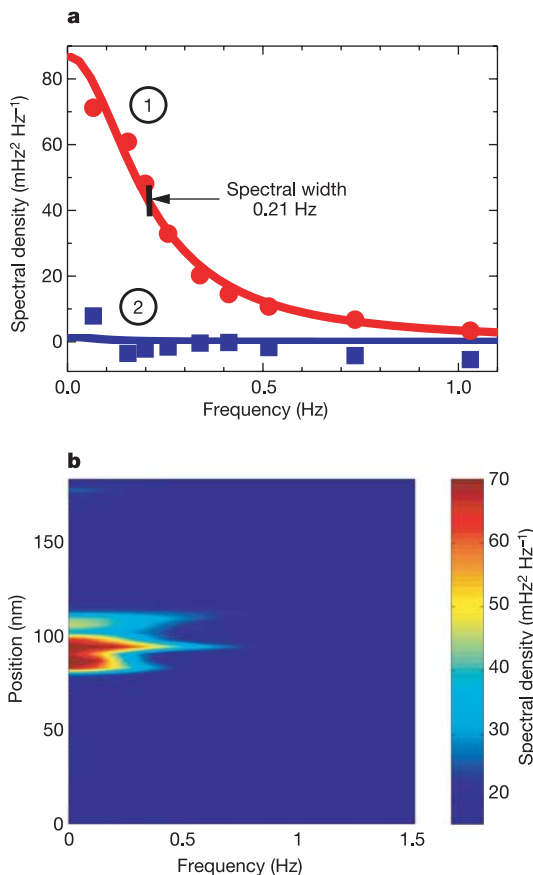


**Figure 4** By measuring the spin signal energy as a function of detection bandwidth, the power spectral density of the spin signal amplitude  $\Delta f_1(t)$  can be determined. **a**, Spectral density for the two positions indicated in Fig. 3. The strong spin signal at position 1 has a narrow spectral width (0.21 Hz), reflecting the long (760 ms) correlation time obtained using iOSCAR spin manipulation. The data are well fitted by a Lorentzian function (solid curve). At position 2, approximately 70 nm away from the position of the spin signal, the spectral density is negligible. **b**, False-colour plot showing power spectral density as a function of position. The spin signal is localized both spatially and spectrally. The data were interpolated between discrete measurement positions to create a smooth image. The apparent fine structure in the signal region is probably an artefact of the limited signal-to-noise ratio of the original data.

increase in field gradient (for example, five times larger) will dramatically speed up the acquisition time and thereby enable two- and three-dimensional imaging applications. (Because we average signal energy, rather than amplitude, the averaging time will decrease as the inverse fourth power of the gradient in the limit of low signal-to-noise ratio.) If the measurement time can be reduced below  $\tau_m$ , real-time readout of the spin quantum state will become possible, enabling a wide variety of quantum measurement experiments. For molecular imaging applications, extension to single nuclear spin detection is necessary, but this will require a roughly 1,000-fold improvement in magnetic moment sensitivity. Considering that the present experiment represents a sensitivity improvement of  $10^7$  times over the original MRFM experiment<sup>29</sup>, the remaining required improvement does not seem out of the question, especially since there is still considerable leeway for increasing the field gradient and lowering the operating temperature. □

Received 16 April; accepted 17 May 2004; doi:10.1038/nature02658.

- Ciobanu, L., Seeber, D. A. & Pennington, C. H. 3D MR microscopy with resolution  $3.7 \mu\text{m}$  by  $3.3 \mu\text{m}$ . *J. Magn. Reson.* **158**, 178–182 (2002).
- Blank, A., Dunnam, C. R., Borbat, P. P. & Freed, J. H. High resolution electron spin resonance microscopy. *J. Magn. Reson.* **165**, 116–127 (2003).
- Sidles, J. A. Folded Stern–Gerlach experiment as a means for detecting nuclear magnetic resonance in individual nuclei. *Phys. Rev. Lett.* **68**, 1124–1127 (1992).
- Sidles, J. A. *et al.* Magnetic resonance force microscopy. *Rev. Mod. Phys.* **67**, 249–265 (1995).
- DiVincenzo, D. P. Two-bit gates are universal for quantum computation. *Phys. Rev. A*, **51**, 1015–1022 (1995).
- Berman, G. P., Doolen, G. D., Hammel, P. C. & Tsifrinovich, V. I. Solid-state nuclear-spin quantum computer based on magnetic resonance force microscopy. *Phys. Rev. B* **61**, 14694–14699 (2000).
- Stowe, T. D. *et al.* Attonewton force detection using ultrathin silicon cantilevers. *Appl. Phys. Lett.* **71**, 288–290 (1997).
- Chui, B. W. *et al.* Mass-loaded cantilevers with suppressed higher-order modes for magnetic resonance force microscopy. *Technical Digest 12th Int. Conf. on Solid-State Sensors and Actuators (Transducers'03)* 1120–1123 (IEEE, Piscataway, 2003).
- Stipe, B. C. *et al.* Electron spin relaxation near a micron-size ferromagnet. *Phys. Rev. Lett.* **87**, 277602 (2001).
- Mozyrsky, D., Martin, I., Pelekhov, D. & Hammel, P. C. Theory of spin relaxation in magnetic resonance force microscopy. *Appl. Phys. Lett.* **82**, 1278–1280 (2003).
- Berman, G. P., Gorshkov, V. N., Rugar, D. & Tsifrinovich, V. I. Spin relaxation caused by thermal excitations of high-frequency modes of cantilever vibration. *Phys. Rev. B* **68**, 094402 (2003).
- Hannay, J. D., Chantrell, R. W. & Rugar, D. Thermal field fluctuations in a magnetic tip—implications for magnetic resonance force microscopy. *J. Appl. Phys.* **87**, 6827–6829 (2000).
- Mamin, H. J., Budakian, R., Chui, B. W. & Rugar, D. Detection and manipulation of statistical polarization in small spin ensembles. *Phys. Rev. Lett.* **91**, 207604 (2003).
- Castle, J. G., Feldman, D. W., Klemens, P. G. & Weeks, R. A. Electron spin-lattice relaxation at defect sites: E' centers in synthetic quartz at 3 kilo-Oersteds. *Phys. Rev.* **130**, 577–588 (1963).
- Albrecht, T. R., Grütter, P., Horne, D. & Rugar, D. Frequency modulation detection using high-Q cantilevers for enhanced force microscope sensitivity. *J. Appl. Phys.* **69**, 668–673 (1991).
- Slichter, C. P. *Principles of Magnetic Resonance*, 3rd edn, 20–24 (Springer, Berlin, 1990).
- Berman, G. P., Kamenev, D. I. & Tsifrinovich, V. I. Stationary cantilever vibrations in oscillating-cantilever-driven adiabatic reversals: Magnetic-resonance-force-microscopy technique. *Phys. Rev. A*, **66**, 023405 (2002).
- Berman, G. P., Borgonovi, F., Goan, H.-S., Gurvitz, S. A. & Tsifrinovich, V. I. Single-spin measurement and decoherence in magnetic-resonance force microscopy. *Phys. Rev. B* **67**, 094425 (2003).
- Brun, T. A. & Goan, H.-S. Realistic simulations of single-spin nondemolition measurement by magnetic resonance force microscopy. *Phys. Rev. A*, **68**, 032301 (2003).
- Davenport, W. B. & Root, W. L. *An Introduction to the Theory of Random Signals and Noise* 104 (McGraw-Hill, New York, 1958).
- Ting, M., Hero, A. O., Rugar, D., Yip, C.-Y. & Fessler, J. A. Electron spin detection in the frequency domain under the interrupted oscillating cantilever-driven adiabatic reversal (iOSCAR) protocol. Preprint at <http://xxx.lanl.gov/abs/quant-ph/0312139> (2003).
- Manassen, Y., Hamers, R. J., Demuth, J. E. & Castellano, A. J. Direct observation of the precession of individual paramagnetic spins on oxidized silicon surfaces. *Phys. Rev. Lett.* **62**, 2531–2534 (1989).
- Durkan, C. & Welland, M. E. Electronic spin detection in molecules using scanning-tunneling-microscopy-assisted boron-spin resonance. *Appl. Phys. Lett.* **80**, 458–460 (2002).
- Wrachtrup, J., von Borczyskowski, C., Bernard, J., Orritt, M. & Brown, R. Optical-detection of magnetic resonance in a single molecule. *Nature* **363**, 244–245 (1993).
- Köhler, J. *et al.* Magnetic resonance of a single molecular spin. *Nature* **363**, 242–244 (1993).
- Jelezko, F. *et al.* Single spin states in a defect center resolved by optical spectroscopy. *Appl. Phys. Lett.* **81**, 2160–2162 (2002).
- Elzerman, J. M. *et al.* Single shot read-out of an individual electron spin in a quantum dot. *Nature* (in the press).
- Jiang, H.-W., Xiao, M., Martin, I. & Yablonovitch, E. Electrical detection of electron spin resonance of a single spin in the SiO<sub>2</sub> of a Si field effect transistor. *Nature* (in the press).
- Rugar, D., Yannoni, C. S. & Sidles, J. A. Mechanical detection of magnetic resonance. *Nature* **360**, 563–566 (1992).

Supplementary Information accompanies the paper on [www.nature.com/nature](http://www.nature.com/nature).

**Acknowledgements** We thank J. Sidles, A. Hero, M. Ting, G. Berman, I. Martin, C. S. Yannoni and T. Kenny for discussions, and D. Pearson, Y. Hishinuma, M. Sherwood and C. Rettner for technical assistance. This work was supported by the DARPA Three-Dimensional Atomic-Scale Imaging programme administered through the US Army Research Office.

**Competing interests statement** The authors declare that they have no competing financial interests.

**Correspondence** and requests for materials should be addressed to D.R. (rugar@almaden.ibm.com).

## Formation of zirconium metallic glass

Jianzhong Zhang & Yusheng Zhao

LANSCE Division, Los Alamos National Laboratory, Los Alamos, New Mexico 87545, USA

Bulk metallic glasses are commonly produced by the rapid cooling of liquid alloys<sup>1</sup>. They have emerged over the past decade as a novel class of materials, with attractive properties and technological promise<sup>1,2</sup>. The bulk metallic glasses so far produced contain three or more component elements<sup>3,4</sup>. These complex compositions are necessary to frustrate the crystallization of the liquid melt on cooling, but can also lead to phase separation, which is detrimental to the thermal and mechanical properties of metallic glasses<sup>5–8</sup>. Here we report, using X-ray diffraction measurements, the formation of a bulk metallic glass from elemental zirconium at high static pressures and low temperatures (relative to its melting temperature at atmospheric pressure). Amorphous zirconium can be recovered at ambient conditions and demonstrates a superior thermal stability compared to amorphous alloys<sup>3,9</sup>, which could lead to new high-temperature applications of amorphous metals.

In multi-component systems, glass-forming ability (GFA) is viewed as the resistance to precipitation of crystalline phases from supercooled liquid metals<sup>10</sup>, and alloys with high GFA all have three common features<sup>3,4</sup>: (1) they consist of at least three components; (2) there is significant mismatch of the atomic size of the constituent elements; and (3) there are negative heats of mixing among the major alloying elements. Addition of elements that are chemically and topologically different from the other species not only creates an energy barrier for nuclei to form but also effectively increases melt viscosity or fragility, which results in a reduced rate of both nucleation and growth and an increase in GFA. The production of bulk glassy materials in pure metals, however, remains a long-standing scientific curiosity and technological interest. The difficulties arise from the facts that the equilibrium melt viscosity of pure metals is three orders of magnitude smaller than that of amorphous alloys<sup>11</sup> and that current technology has yet to reach a cooling rate in excess of the  $10^{10} \text{ }^\circ\text{C s}^{-1}$  that is needed to make pure metals amorphous<sup>12</sup>.

We studied zirconium metal at pressures and temperatures up to 17 GPa and 1,000 °C, using energy-dispersive synchrotron X-ray diffraction and time-of-flight neutron scattering. In X-ray diffraction experiments, we used both DIA-type<sup>13</sup> and T-cup<sup>14</sup> large-volume high-pressure apparatus installed at Brookhaven and Argonne National Laboratories. Neutron scattering experiments were performed using a high-pressure/high-temperature (high  $P$ – $T$ ) cell assembly<sup>15</sup> in a TAP-98 toroidal-anvil press at Los Alamos Neutron Scattering Center. The starting sample of zirconium has a close-packed hexagonal structure ( $\alpha$ -phase) and is of extremely high purity, with 35 p.p.m. Hf, less than 25 p.p.m. of C, N and Al,